

# A wireless powered LED marker for Intraoperative Localization

Jingjing Luo

Technische Universiteit Delft

# A wireless powered LED marker for Intraoperative Localization

by

**Jingjing Luo**

in partial fulfillment of the requirements for the degree of

**Master of Science**  
in Biomedical Engineering

at the Delft University of Technology,  
to be defended publicly on Wednesday September 27th, 2017 at 14:00.

Supervisor:	Prof. J. Dankelman	
	Prof. B. Hendriks,	Philips
Thesis committee:	Prof. B. Hendriks,	Philips
	Prof. J. Dankelman,	TU Delft
	Dr. V. Giagka,	TU Delft

*This thesis is confidential and cannot be made public until September 27, 2022.*

An electronic version of this thesis is available at <http://repository.tudelft.nl/>.

# Preface

This project was for me, a good representation and practice of how interdisciplinary knowledge can be connected. It started by discovering one of the current problems in clinical area. Followed by a broad-scale literature study exploring the current technologies and possible solutions. Finally, the prototype realization and experiments were carried out. This process involves fields of electronics design, electromagnetism, simulation set-up, biology, mathematics, and the measurement design in a laboratory environment. It provided me a chance to have a deeper understanding on the role and the responsibility of a Biomedical Engineer, which is to apply the engineering skills to solve clinical challenges more efficiently.

This study is presented in the form of article. The main article shows the experiments of the final system. In order to maintain the conciseness of the main article, extra works and proposals considered to be too expatiatory to include were further elaborated in the Appendices.

I would like to thank my supervisors and friends for their enormous help and supports. Finishing this project would be more difficult without the professional guidance from my supervisor Benno Hendriks and Jenny Dankelman. During my internship in Philips, Gert Doodemon provides many inspiring advises on the experimental set-up. I would also like to thank my friends Ron and Hardi for the encouragement and company throughout the project.

*Jingjing Luo  
Delft, September 2017*

# A wireless powered LED marker for Intraoperative Localization

J. Luo

Biomedical Engineering

Dept. Mechanical, Maritime and Materials Engineering

Delft University of Technology

Delft, Netherlands

**Abstract**—Intraoperative Localization plays an important role in achieving a safe and successful resection surgery. Conventionally, Intraoperative Localization techniques rely on intraoperative imaging guidance, radioactivity guidance, and fluorescence guidance together with local markers. These techniques can assist the surgeon by accurately finding the lesion in the operating room. In this article, an idea of using wireless powered LED marker as a more intuitive alternative is proposed, mainly inspired by the rapid developments in microelectronics and wireless power transfer techniques. This paper presents a complete system using a wireless powered LED marker that can be used for intraoperative localization. The operating frequency and source current density distribution were determined based on the Mid-field wireless power transfer theory. The results were simulated with muscle and multilayered breast tissue model in FEKO. During implementation, the transmitter is approximated by using a two-port antenna which operates at around 2Ghz. The size of the LED marker was minimized by using a double layer PCB design. The energy harvesting component is a 5-turn coil, which reduces the resonant frequency of the entire marker when it is wound around the PCB. The PCB is coated with biocompatible material. Finally, the system is tested and verified using media of air, tissue simulating liquid, butter, and swan lung tissue. It can be concluded that this system can potentially increase the convenience and accuracy of intraoperative localization.

**Keywords**—Intraoperative localization, LED marker, wireless power transfer, EM simulation, coil, resonant frequency.

## I. INTRODUCTION

In the past few decades, the rapid development of medical imaging techniques have significantly improved the accuracy of cancer diagnosis. Visualizing and localizing the lesion using Computer tomography (CT), Magnetic resonance imaging (MRI), and Radiographic Imaging have formed an important part in preoperative

localization and remains the main reference for the surgeon to localize the lesion during surgery. Despite the high precision of imaging techniques, achieving highly accurate intraoperative localization still remains a challenge[1].

An intraoperative localization system consists of a marker placed inside the body and a detector placed outside the body. The surgeon relies on the location of the marker to identify the lesion. The marker uses either a radiation signal, a structural signal, or an optical signal for detection. Radionuclides marker such as Technetium-99m, Fluorine-18, and Iodine-125 carry the radiation signal that is detected by gamma probes after injection[2]. Structural signal detection is realized by inserting a metallic marker that is visible under fluoroscopy[3]. Optical signals are gradually gaining more attention due to its intuitive visual guidance. Chemical markers including fluorescein, 5-aminolevulinic acid (5-ALA), and Indocyanine green(ICG), Methylene Blue(MB) have been used as the fluorophore that emits light. The system called Near infrared imaging fluorescence (NIRF) is mostly studied due to the higher tissue penetration ability of NIR light as compared to that of visible light, but it requires a dedicated camera as the detector. There have been recent attempts on coupling antibodies with fluorophores to realize a target-specific localization for improved accuracy[4][5][6].

Even though there is a huge potential for fluorophores to work as a fluid optical marker, several challenges remain to be solved. Before reaching the targeted site, the injected fluid will require some time for a sufficient body uptake which highly depends on the dose and concentration. A high concentration is needed for MB to gain sufficient visibility, bringing about a concern of cytotoxicity[7]. The only two FDA approved fluorophores ICG and MB used in NIRF, are reported



unsuitable to couple specific antibodies, result in a high background fluorescence signal[8]. As for the external detector, computing and a dedicated camera are required for NIRF which makes it more complicated and costly to develop. Furthermore, the fluorescence remains on the surface of the lesion and cannot be seen from the skin level.

One alternative to overcome the disadvantages above is to use a solid marker that can self-emit light with higher brightness. Light emitting diode(LED) is a two-lead semiconductor light source which can be made at micro-millimeter scale with high output power. More importantly, its optical signal can be detected by the naked eye thus no external detector is required.

In the field implantation, LEDs are mainly used in the research of optogenetics, which is a technique that uses light to trigger cellular activity[9]. There is also an example of using LED with a cable as an intraoperative marker at very shallow skin level in Microdochectomy [10]. There are several benefits of using LED as a solid marker: precise location, flexible surgical planning, complete removability, and the lower requirement for clinical approval. Furthermore, it can be placed in any targeted tissue without much concerns of selective absorption. The disadvantage of marker migration can be potentially improved by adjusting the shape. For example, RF pulse transponder are more likely to move due to its smooth surface and grain-like shape[11], whereas the metal hooked-wire marker has a greater performance on stability due to the hook at the tip[12].

The next question was on how to power up the LED marker inside the tissue. Various power supply techniques for implantable devices have been studied focusing on thin-film battery, biofuel cells, and wireless power transfer using acoustic wave or electromagnetic wave[13][14]. In 2013, a study introduced the concept of Mid-field wireless power transfer demonstrating that the optimal power transfer efficiency occurs at low GHz frequency range and is suitable for powering millimeter-sized implants without exceeding the EM exposure requirements [15].

In this paper, a complete intraoperative localization system using wireless powered LED marker is presented. The theory of Mid-field wireless power transfer has been adapted in the design. The energy harvesting component is a 5-turn coil connected to the circuit that resonate at around 1.9GHz. A four-port antenna was implemented as part of transmitter but only 2 ports were used for

higher controllability. The system was tested with the media of air, tissue simulating liquid, butter, and swan lung tissue at a 3cm distance between the antenna and the LED marker. This is the first time a wireless powered LED was used as an intraoperative localization marker.

## II. METHODOLOGY

### A. Simulation set-up

The simulation starts from calculating the optimal frequency and source current density distribution in Matlab. The optimization process is based on Mid-field wireless power transfer (WPT) theory[15]. The Mid-field WPT theory states that when the transmitter and receiver separated by several centimeters distance and operating at low GHz frequency range, the quasistatic approximation is removed. The losses seen here are mainly due to tissue relaxation rather than the radiative losses and Ohmic losses. As a result, the coupling factor can be defined as the ratio of received power from the induced *emf* to the tissue relaxation losses[for the theory see Appendix A].

Based on field equivalence principle [16], one can represent the *E* field and *H* field from the source with a current density distribution by applying Green's function. The optimal operating frequency and current density distribution are found when the coupling factor is maximum. [for more detailed codes see Appendix B]

In the simulation, both muscle tissue and multilayered breast tissue were used. The multilayered breast tissue consists of three layers: skin, fat, gland(2mm, 15mm, 15mm), as shown in Fig.1. The receiver was set at 3cm under the skin. The size of the marker was designed to be only millimeter-sized(1mmx3mmx20mm), hence it was assumed that the gland and other layers of tissue are infinite layers for computational simplicity. This assumption was later corrected in EM simulation software with a finite dimension. The dielectric properties of tissue are represented using Cole-Cole model[17].

After obtaining the operating frequency and optimal source current density distribution, the model was further processed into the Electromagnetic simulation software FEKO 2017(Altair). Several attempts were made to translate the current density distribution calculated in Matlab into FEKO simulation, however, most were found to be inaccurate[see Appedix C]. On the other hand, there is currently no standard method for designing an antenna using only the current density distribution. Therefore, the equivalent source EM field was extracted from Matlab

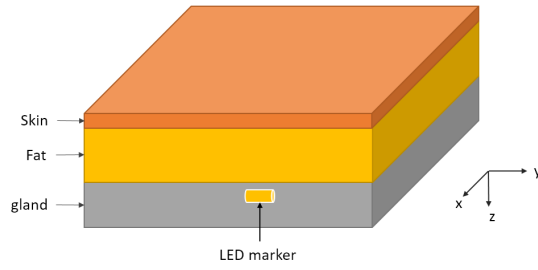


Fig. 1: Simplified multilayered breast tissue model with implanted LED marker.

and translated into FEKO to represent the source directly. Later, for a more realistic simulation, an existing antenna design proposed in [18] was used. This antenna has a partly similar current distribution as the optimal one. In the simulation, the total input power was set to be 500mW, the main output calculated were the near-field radiation pattern, Specific Absorption Rate(SAR), and S11 (S-parameter) of the antenna.

SAR is a measure of the rate at which energy is absorbed by the human body when exposed to a radio frequency (RF) electromagnetic field. Till date, there has been no established safety guideline for medical applications utilizing wireless power. However, according to IEEE C95.1 2005[19], ICNIRP 1998 (0 Hz - 300 GHz) [20], the EM field exposure with human control should meet the following requirements:

- Whole-body average SAR should be less than 0.4 W/kg
- Maximum local SAR, averaged over 10 g of tissue, should be less than 10 W/kg

### B. Transmitter and Receiver design

The antenna shown in Fig.2 has four coaxial cables that work as four individual inputs, 4 metal circular paths on the top layer and a patterned metal plate on the bottom layer. By assigning a conjugated phase of four individual input signals[21], a circular current path can be created on the metal plate which then radiates focused electromagnetic waves by means of constructive interference. The original antenna, which has a 1.7mm substrate, operates at around 1.55GHz and 1.9GHz tested by FEKO as shown in Fig.4. This operating frequency can be tuned by adjusting the thickness of the substrate. To assign different phases, a phase shifter was connected

between the signal generator and the antenna, as shown in Fig.3.

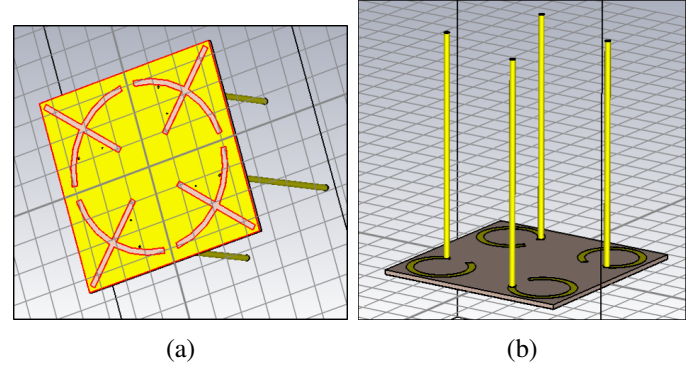


Fig. 2: (a) The bottom view of the antenna model; (b) The top view of the antenna model.

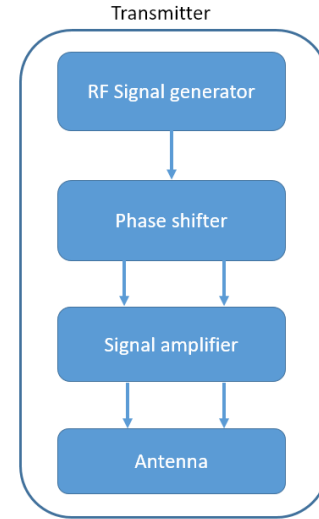


Fig. 3: The block diagram of the transmitter system.

The circuit of the LED marker is shown in Fig.5. The marker works as an implant, a receiver, and a light emitter. Hence there are several basic requirements:

- 1) Energy harvesting capability,
- 2) Small size,
- 3) Biocompatibility,
- 4) Visible to naked eye.

The LED marker design discussed in detail as follow is based on these requirements.

1) *Energy harvesting:* The LED is the load at the receiver end in this two-port wireless power transfer

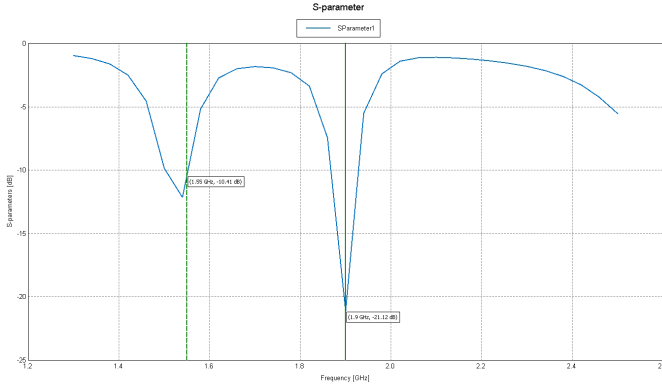


Fig. 4: The S11 parameter of the antenna. Two peaks occur at 1.55GHz with -10.41dB and at 1.9GHz with -21.12dB respectively.

system shown in Fig.6. A 5-turn coil is used as the receiver part that converts magnetic energy into the induced electrical energy. The following functional circuits rectify and multiply the low AC input voltage so that sufficient voltage can reach the load (LED). The adjustable parameters in the functional circuits to obtain sufficient voltage at the load are the numbers of stage of the voltage multiplier, capacitance values, and resistance of Schottky diode[for more details see Appendix E].

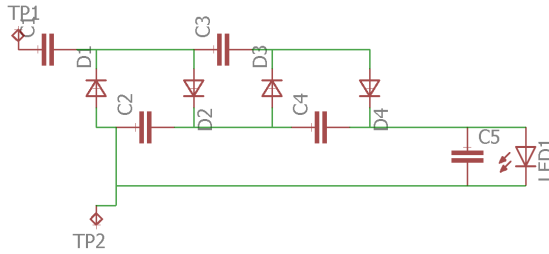


Fig. 5: The circuit on the PCB. There are a four-stage of voltage multiplier, a ripple-removing capacitor, and the LED.

2) *Small size*: The PCB design was performed in Eagle(Autodesk). A double-layer PCB was used in order to minimize the size of the LED marker shown in Fig.7. Having a matched operating frequency between the transmitter and the receiver is critical to achieve optimal power transfer efficiency. A 5-turn coil was connected to the PCB to harvest energy. Two coil configurations were investigated for their resonant frequency, the first type was to separate the coil from the PCB which would

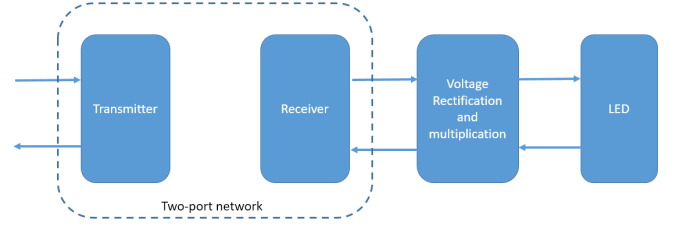


Fig. 6: The block diagram of the wireless power transfer system of the LED marker. The coil is the receiver part in the two-port network, connected by functional circuit and the LED.

result in a bigger size, and the second configuration was to have the coil wound around the PCB which would minimize the size. Next, a method to investigate the operating frequency of one receiver is carried out using a network analyzer with a small loop antenna which has an extremely high self-resonant frequency(SRF). While the network analyzer was measuring the S11 parameter of the loop antenna, the receiver was placed closer to the loop for energy coupling as shown in Fig.8, the change in the S11 parameter directly corresponds to the resonant frequency of the receiver.

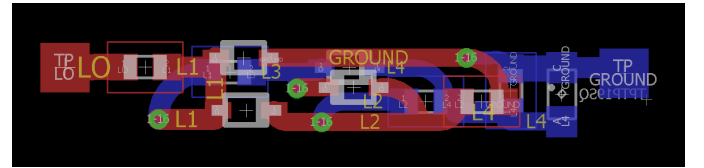


Fig. 7: Double layered PCB design diagram. The red path forms the top layer, whereas the blue paths forms the bottom layer. Electrical connection between the layers is realized by the conductive holes on the PCB.

3) *Biocompatibility*: Good biocompatibility ensures the flexibility of surgical planning by allowing the marker to stay inside the body a longer time. Conventional coating such as Parylene and epoxy resin can be used to render biocompatibility and also act as electrical insulation to the marker. Collagen can also be used for the outer coating as it expands its size significantly by quickly absorbing surrounding fluid. It has been used as the coating of breast biopsy markers in the industry[22]. Expanding the size increases the stability of the marker inside the tissue. In this study, the ‘Norland Optical Ad-

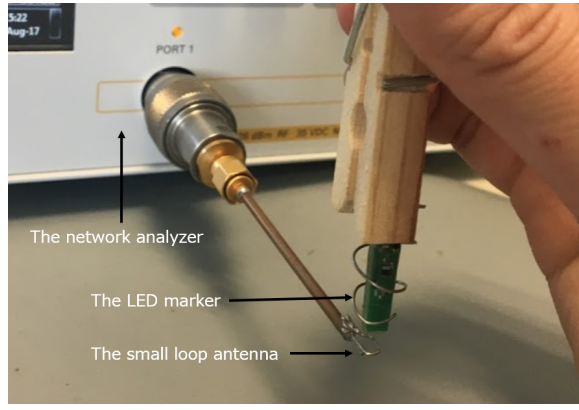


Fig. 8: Resonant frequency measurement of the LED marker by placing the marker close to a small loop antenna. The change of the S11 parameter of the loop antenna directly reflect the resonant frequency of the marker on the network analyzer.

hesive 72' [23] was used, which is a transparent coating material only for the purpose of electrical insulation.

4) *Visibility*: The process of refraction and reflection is intense in organic substrates, which is responsible for the dispersion of light in tissue. Within the wavelength range of visible light, the penetration ability is proportional to the wavelength, as shown in Fig.9. In order to maximize the detectability of the light from the marker, red color LED (620nm-750nm) was chosen.

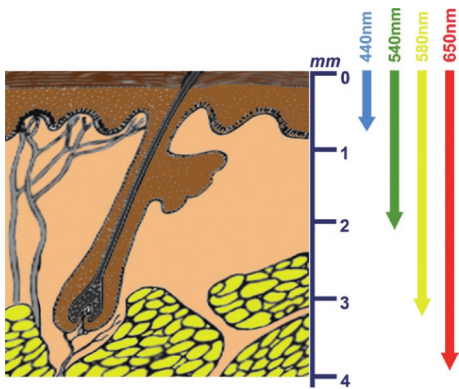


Fig. 9: Tissue penetration ability of different wavelengths within visible light range [24].

### C. Experimental set-up

The experimental set-up consists of the LED marker and the transmitter with medium in between. Before

insertion, the LED marker was completely insulated to avoid direct contact with medium. The various test media included air, tissue simulating liquid, butter, and a swan lung tissue. The tissue simulating liquid(MSL2450V2, Speag) has the equivalent dielectric properties, including relative permittivity and conductivity, as human muscle at a RF frequency range up to 2.7GHz. The liquid was filled in a transparent plastic box with around 3 cm to 3.5 cm depth as shown in Fig.10. To further verify the visibility of the LED light, the LED marker also placed inside a slab of butter and inside the swan lung tissue.

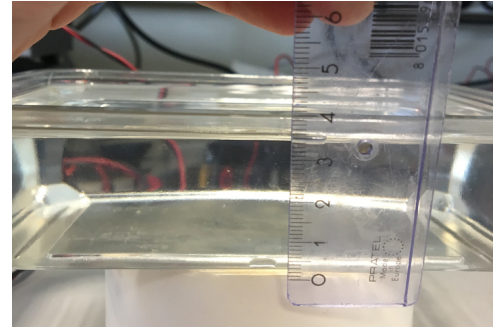


Fig. 10: The depth of tissue simulating liquid in the box is between 3 cm to 3.5 cm.

## III. RESULT

### A. Simulation result

Fig.11 illustrates the 21-by-21 matrix of current density distribution that radiates at 2GHz. The current density distribution starts from the middle and shunts to lateral direction to form two semi-circular paths. This distribution changes with operating frequency and tissue type. In multilayered breast model, the coupling efficiency is much higher at GHz range and reaches maximum at 2.8GHz.

The equivalent EM field radiated from the current density distribution produces a focusing magnetic field in the multilayered tissue as shown in Fig.12. The focal area can be seen on the cross section (XY axis). The directional field (red arrows) suggests that the coil should be oriented along X axis to harvest the magnetic energy. Unlike the conventional 2-coil inductive coupling system where magnetic flux should be produced vertically (Z axis), the magnetic field in this configuration is produced horizontally(X axis). It can be inferred that the performance of energy coupling will be sensitive to the relative orientation between the coil and the transmitter.

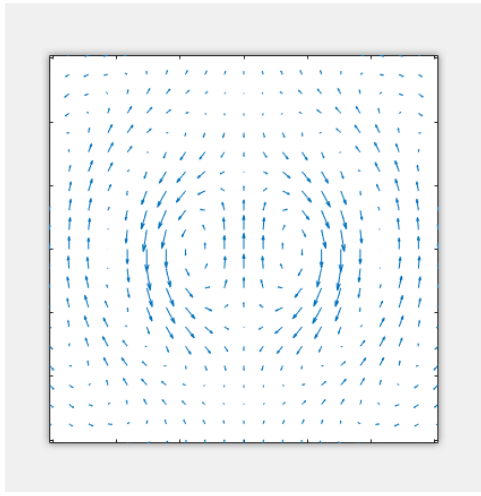


Fig. 11: The current density distribution that represent the source for multilayered breast tissue model.

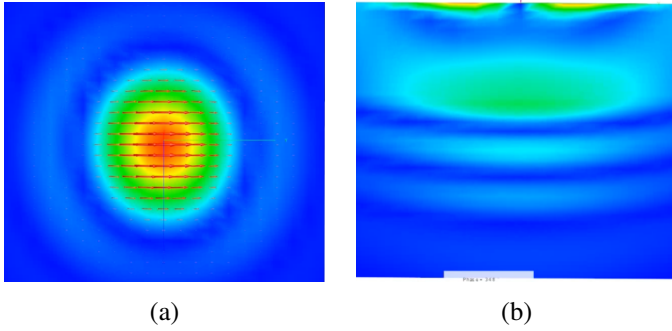


Fig. 12: The simulation result of the magnetic field produced by equivalent source EM field. (a) The magnetic field on XY plane at 3cm depth is shown, the direction of the field is transverse; (b) The magnetic field on YZ plane is shown, there's a focusing effect the field

The simulation result of using the antenna is shown in Fig.13 . The magnetic field in the tissue without conjugated phase assignment is not focused as shown in Fig13a, By having the same phase, no constructive interference occurs. On the other hand, by assigning the two signals diagonally with a 180-degree phase difference, the focusing effect starts to appear as shown in Fig.13b. The direction of the magnetic field on the cross section was parallel to the diagonal line of the XY plane depicted in Fig.13c.

The magnetic field under multilayered tissue also has the focusing effects, as shown in Fig.14. After the

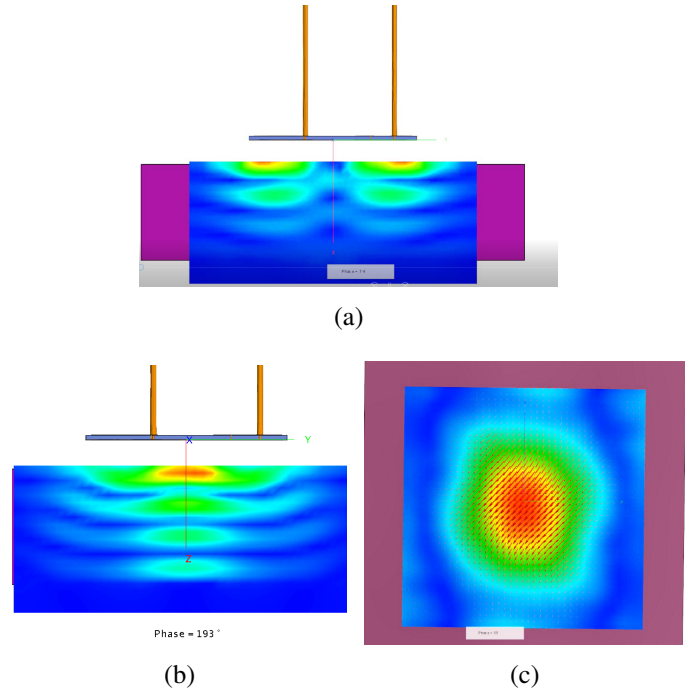


Fig. 13: The Magnetic field inside the tissue produced by the antenna. (a) The magnetic field has no focused effect when the input signal has no phase difference;(b) The magnetic field appears a focused effect when the input signal has a 180-degree phases difference; (c) The magnetic field on XY plane has diagonal direction in the focal area.

size of the gland layer is adjusted to a more realistic volume, the peak SAR for 10g tissue from the simulation result is found to be 3.84W/kg, which is below the regulated threshold (10W/kg). The peak value appears on the fat layer as shown in Fig.15. Assuming the weight of a patient is 70kg, the Whole-body average SAR is 0.00714W/kg, which is drastically lower than the regulated value of 0.4 W/kg. Hence, the configuration meets the safety requirements.

### B. Implementation results

The final antenna and receiver are shown in Fig.16. The optimal operating frequency of the antenna was measured to be at 1.6GHz and 2Ghz respectively by using a network analyzer, which are close to the simulation result depicted in Fig.4.

As for the receiver, it was expected that due to the slightly shorter wire length, the resonant frequency of the marker with wound coil should be higher than that



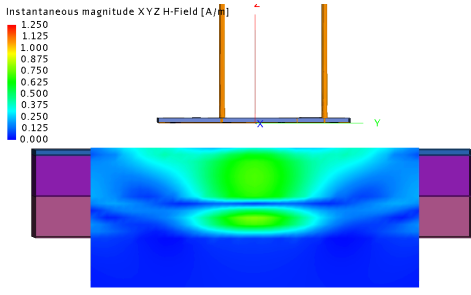


Fig. 14: The simulation result of the focused magnetic field in the Multilayer breast model.

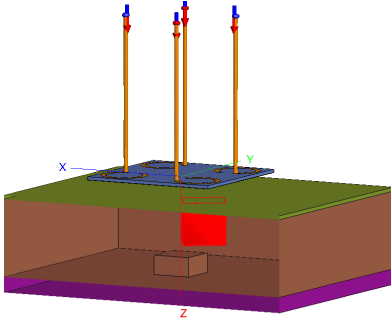


Fig. 15: The peak 10g average SAR appears in the fat layer in the model, corresponding to 3.84W/kg.

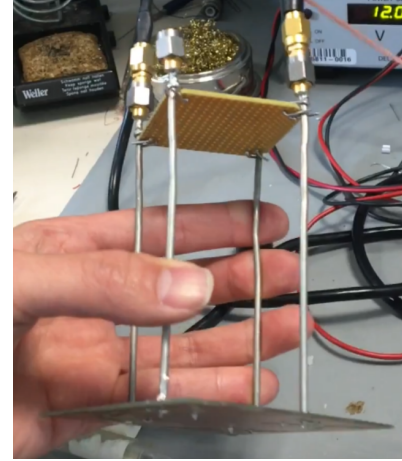
of the marker with a separated coil. However, the result was the opposite: The marker with wound coil had a much lower resonant frequency of 560MHz than that of another marker with separate coil of 1.98GHz. This is caused by the change of the distance between the coil and the conductive materials on the PCB. Another test was conducted to confirm the hypothesis [see Appendix D]. This distance change may bring in two factors that affect the resonant frequency:

- 1) The extra parasitic capacitance created between the coil and the PCB,
- 2) The variation in the electrical length of the coil due to the coating material.

The extra parasitic capacitance is created at high frequency when the coil is very close but not in contact with the conductive material on PCB, such as the soldering pads. When powered, they are affected by each other's electric field and store opposite electric charges like a capacitor. The value of capacitance is determined by distance, operating frequency, the diameter of the coil,



(a)



(b)

Fig. 16: The manufactured antenna. (a) The bottom layer; (b) The four input feed.

and material types. If one simplifies the circuit of the LED marker to that of an LC tank with a load, the increased capacitance will directly decrease the resonant frequency. On the other hand, based on the transmission line theory[25], filling dielectric material between conductor increases the electrical length or lowers the velocity of the transmitted signal by a velocity factor that is inversely proportional to the square root of the dielectric constant. The coating material used in this study has a low dielectric constant[23], thus the effect should be less significant compared to that from the first factor.

Even though having a coil wound around PCB significantly decreases the dimension of the marker, its frequency behavior becomes less predictable due to the two aforementioned factors, which in turn decreases the controllability in matching the frequency between the transmitter and the receiver. Hence, the marker with separated coil was used in the following experimental



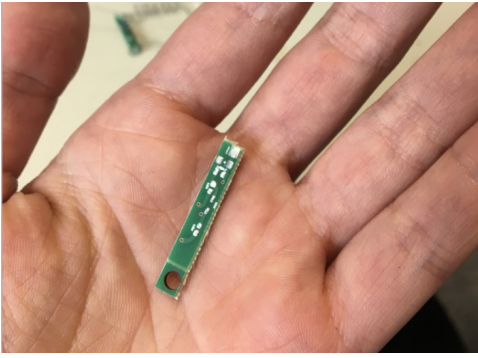


Fig. 17: The receiver PCB.

phase since its resonant frequency at 1.98GHz is more stable and predictable.

### C. Experimental results

The experimental results demonstrate that the LED marker can light up both under air and tissue simulating liquid, inside the butter and swan lung tissue, as depicted in Fig.18. The antenna operates at 1.9-2.0GHz which matches the resonant frequency of the LED marker, this ensures optimal power transfer efficiency. With the same input power (9dBm), the LED is more visible under butter than in lung tissue. This suggests that the LED marker may be able to provide enough optical guidance when it is inserted in fatty tissue which is similar to the butter. However, when inserted into a much denser medium such as lung tissue or muscle, a higher power LED or multiple LEDs could be used for a improved visibility. The difference in visibility is due to the variants in optical properties among different tissues, it is thus beneficial to quantify the relation between the visibility of a implanted LED marker versus the input power of the LED in different tissue.[see Appendix F]

The experimental results also matches the inferences obtained from the simulation results, suggesting that the system is sensitive to relative orientation as shown in Fig.19. The LED is brightest when the coil is parallel to the diagonal line(between the two input feed) of the antenna. Even if four-port inputs were used instead of two-port, the high directional sensitivity would remain. Since the focal point is determined by the input phase difference, one can use programmable control over the input phase to create a rotating magnetic field, as a potential solution to reduce the sensitivity.

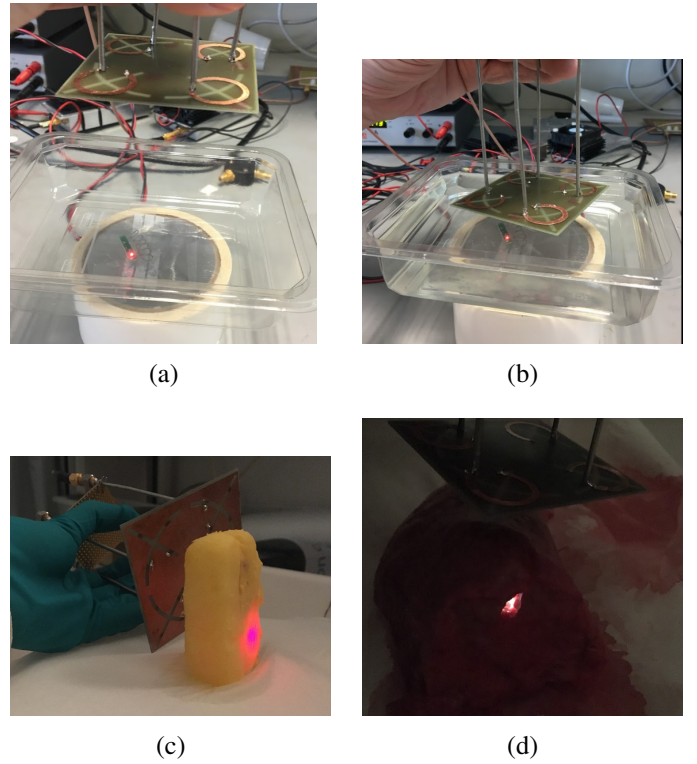


Fig. 18: Experimental results in different medium. In(a) and (b), the LED marker was able to light up in the air and under the tissue simulating liquid; In (c) and (d), the LED marker was able to light up inside both the butter and the swan lung, but the light in the butter is seen to be more visible.

## IV. CONCLUSION

Intraoperative localization using optical guidance has gained more attention because of its ability to restore the visual interpretation for the surgeon. Conventionally, it was mainly done using fluorophores in a fluid form with a dedicated camera detector. The LED marker in this paper, which is a combination of optical guidance and a solid marker, compensates for the drawbacks of the fluid optical marker. At the same time, Mid-field wireless power transfer theory provides a solution for wireless power supply.

In this paper, an intraoperative localization system using wireless powered LED marker is proposed and tested. The optimal operating frequency and source current density distribution were calculated for multilayered breast tissue simulation model. The results were further translated into a EM simulation software and the source was replaced by an existing antenna. The circuit on the

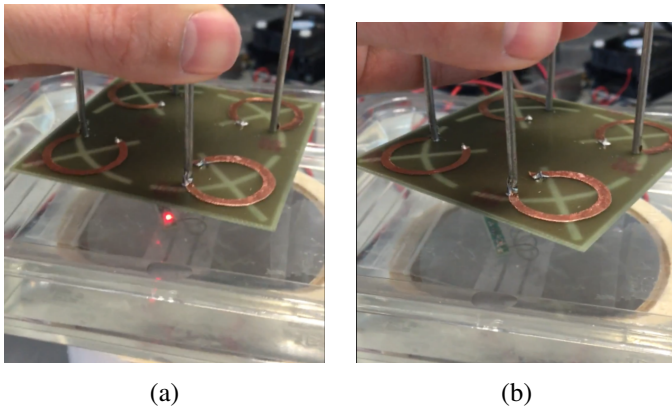


Fig. 19: Directional sensitivity. (a) The LED marker was able to light up when the coil is parallel to the diagonal line of the antenna; (b) The LED marker was not able to light up when the coil is crossing the diagonal line of the antenna.

LED marker was designed to rectify and multiple the AC voltage harvested by the coil. The final size of the LED marker is minimized using double layer PCB. By connecting the same coil to the PCB in two different configurations, one can obtain two very different resonant frequencies due to the change in parasitic capacitance and electrical lengths. Finally, the LED marker was tested across various media. From a Biomedical perspective, the safety concerns were taken into account by using bio-compatible insulation material and restricting the value of SAR according the guidelines.

Since the optimal current density distribution may vary due to operating frequency and tissue type, it would be beneficial to have an antenna design cater for different current density distributions, thus allows for a customized antenna for different applications. Furthermore, the system can also be improved by using high power LEDs or multiple LEDs for a better detectability, and by using programmable control over the input phase difference to minimize the directional sensitivity.

## REFERENCES

- [1] Singhal S, Nie S, Wang MD. Nanotechnology applications in surgical oncology. *Annu Rev Med* 2010;61:359-73
- [2] Povoski, Stephen P., et al. "A comprehensive overview of radioguided surgery using gamma detection probe technology." *World journal of surgical oncology* 7.1 (2009): 1.
- [3] Marquardt, Gerhard, et al. "Preoperative coil marking to facilitate intraoperative localization of spinal dural arteriovenous fistulas." *European Spine Journal* 18.8 (2009): 1117-1120.
- [4] Gleysteen JP, Duncan RD, Magnuson JS, Skipper JB, Zinn K, Rosenthal EL (2007) Fluorescently labeled cetuximab to evaluate head and neck cancer response to treatment. *Cancer Biol Ther* 6:11811185
- [5] Lee SB, Hassan M, Fisher R et al (2008) Affibody molecules for in vivo characterization of HER2-positive tumors by near-infrared imaging. *Clin Cancer Res* 14:38403849
- [6] Withrow KP, Newman JR, Skipper JB et al (2008) Assessment of bevacizumab conjugated to Cy5.5 for detection of head and neck cancer xenografts. *Technol Cancer Res Treat* 7:6166
- [7] Wainwright, Mark, et al. "Increased cytotoxicity and phototoxicity in the methylene blue series via chromophore methylation." *Journal of Photochemistry and Photobiology B: Biology* 40.3 (1997): 233-239.
- [8] Hong, Guosong, Alexander L. Antaris, and Hongjie Dai. "Near-infrared fluorophores for biomedical imaging." *Nature Biomedical Engineering* 1 (2017): 0010.
- [9] Kim, Tae-il, et al. "Injectable, cellular-scale optoelectronics with applications for wireless optogenetics." *Science* 340.6129 (2013): 211-216.
- [10] Ma, Xiao-Peng, et al. "A Novel Light-Emitting Wire Enhances the Marking and Visualization of Pathologic Mammary Ducts During Selective Microdochectomy." *Annals of surgical oncology* 23.3 (2016): 796-800.
- [11] Willoughby, Twyla R., et al. "Target localization and real-time tracking using the Calypso 4D localization system in patients with localized prostate cancer." *International Journal of Radiation Oncology\* Biology\* Physics* 65.2 (2006): 528-534.
- [12] Sloty Jr, Philipp, et al. "Preoperative Localization of Spinal and Peripheral Pathologies for Surgery by Computed TomographyGuided Placement of a Specialized Needle System." *Neurosurgery* 66.4 (2010): 784-787.
- [13] Amar, Achraf Ben, Ammar B. Kouki, and Hung Cao. "Power approaches for implantable medical devices." *Sensors* 15.11 (2015): 28889-28914.
- [14] Olivo, Jacopo, Sandro Carrara, and Giovanni De Micheli. "Energy harvesting and remote powering for implantable biosensors." *IEEE Sensors Journal* 11.7 (2011): 1573-1586.
- [15] Ho, John S., Sanghoek Kim, and Ada SY Poon. "Midfield wireless powering for implantable systems." *Proceedings of the IEEE* 101.6 (2013): 1369-1378.
- [16] Quijano, Javier Leonardo Araque, and Giuseppe Vecchi. "Field and source equivalence in source reconstruction on 3D surfaces." *Progress In Electromagnetics Research* 103 (2010): 67-100.
- [17] C. Gabriel. *Compilation of the Dielectric Properties of Body Tissues at RF and Microwave Frequencies*, Report N.AL/OE-TR- 1996-0037, Occupational and environmental health directorate, Radiofrequency Radiation Division, Brooks Air Force Base, Texas (USA), 1996.
- [18] The 4-port antenna, <http://web.stanford.edu/group/poongroup/cgi-bin/wordpress/resources/>
- [19] IEEE Standards Coordinating Committee. "IEEE standard for safety levels with respect to human exposure to radio frequency electromagnetic fields, 3kHz to 300GHz." *IEEE C95* (1992).
- [20] International Commission on Non-Ionizing Radiation Protection. "ICNIRP Guidelines for Limiting Exposure To Time-Varying Guidelines for Limiting Exposure To Time-Varying

- Electric, Magnetic and Electromagnetic fields.” *Health Phys* 74 (1998): 494-522.
- [21] Ho, John S., Yuji Tanabe, and Ada SY Poon. ”Midfield Wireless Powering: A Brief Computational Tutorial.” (2015).
  - [22] MammoMARK and CorMARKs,  
<http://www.mammotome.com/mammomark-cormark/>
  - [23] Norland Optical Adhesive 72,  
<https://www.norlandprod.com/adhesives/noa%2072.html>
  - [24] L. Fodor et al., *Aesthetic Applications of Intense Pulsed Light*, DOI: 10.1007/978-1-84996-456-2\_2, Springer-Verlag London Limited 2011
  - [25] Amlaner, Charles J., and David W. Macdonald, eds. *A handbook on biotelemetry and radio tracking: proceedings of an International Conference on Telemetry and Radio Tracking in Biology and Medicine*, Oxford, 20-22 March 1979. Elsevier, 2013.
  - [26] Poon, Ada SY, Stephen O’Driscoll, and Teresa H. Meng. ”Optimal operating frequency in wireless power transmission for implantable devices.” *Engineering in Medicine and Biology Society*, 2007. EMBS 2007. 29th Annual International Conference of the IEEE. IEEE, 2007.
  - [27] Poon, Ada SY, Stephen O’Driscoll, and Teresa H. Meng. ”Optimal frequency for wireless power transmission into dispersive tissue.” *IEEE Transactions on Antennas and Propagation* 58.5 (2010): 1739-1750.
  - [28] Kim, Sanghoek, and Ada SY Poon. ”Optimizations of source distribution in wireless power transmission for implantable devices.” *Antennas and Propagation Society International Symposium (APSURSI)*, 2010 IEEE. IEEE, 2010.
  - [29] Debye, P. (1913), *Ver. Deut. Phys. Gesell.* 15, 777; reprinted 1954 in collected papers of Peter J.W. Debye. Interscience, New York
  - [30] Kim, Sanghoek, and Ada SY Poon. ”Optimal transmit dimension for wireless powering of miniature implants.” *Antennas and Propagation (APSURSI)*, 2011 IEEE International Symposium on. IEEE, 2011.
  - [31] Kim, Sanghoek, John S. Ho, and Ada SY Poon. ”Midfield wireless powering of subwavelength autonomous devices.” *Physical review letters* 110.20 (2013): 203905.
  - [32] Li, Le-Wei, et al. ”Electromagnetic dyadic Green’s function in spherically multilayered media.” *IEEE Transactions on Microwave Theory and Techniques* 42.12 (1994): 2302-2310.
  - [33] The list of dielectric properties of different tissue types,  
<https://www.itis.ethz.ch/virtual-population/tissue-properties/database/dielectric-properties/>
  - [34] User Manual for FEKO 14.0,  
<https://altairuniversity.com/learning-library/user-manual-for-feko-14-0/>
  - [35] Photometer. (2017, May 1). In Wikipedia, The Free Encyclopedia. Retrieved 10:14, September 8, 2017 , from <https://en.wikipedia.org/w/index.php?title=Photometer&oldid=778174211>

## APPENDIX A

### MIDFIELD WIRELESS POWER TRANSFER THEORY

This appendix introduces the mid-field wireless power transfer theory. This theory was proposed to find the optimal configuration of wireless power transfer for a mm-sized implants that is separated from the transmitter by few centimeters distance.

The problem starts from finding the optimal operating frequency for wireless power transfer with biological tissue. Conventional wireless power transfer system mostly operates at below 20MHz based mainly on Near-field coupling theory. The system consists of simple coils for both transmitter and receiver. The field behaviour can be well-explained by applying quasi-static approximation on Maxwell equation:

$$\nabla \times H = -i\omega\epsilon_0\epsilon_r E + \sigma E \quad (1)$$

$$\nabla \times E = i\omega\mu_0 H - J_m \quad (2)$$

where the term  $-i\omega\epsilon_0\epsilon_r E$  in Equation(1) is the displacement current, that are conventionally neglected at low frequency[26].

The field is thus described by diffusion equation[27]. Diffusion equation states that the EM field decays exponentially with the distance inside the tissue, and the depth of diffusion is inversely proportional to the square root of frequency.

However, when the frequency increases, the displacement current of tissue(dielectric material) becomes more significant and cannot be neglected by quasi-static approximation. At the same time, according to Faraday's law, the received power at the coil end is proportional to the rate of change of the imposed magnetic field. This implies that an optimal operating frequency may occur at a higher frequency.

From both[27] and[28], the authors recalculated the maximum induced *emf* from a point source in a full-wave range. The optimal efficiency is the ratio of the received power from the induced *emf* to the tissue losses.

The received power from the induced *emf* and tissue losses are described as follow:

$$P_r = Re \left\{ \frac{1}{2} H^*(-\hat{z}d) \cdot (-i\omega\mu_0 I_r A_r \hat{n}) \right\} \quad (3)$$

$$P_{loss} = \frac{\omega}{2} \int_{z < -d_1} Im \mathcal{E}(r) |E(r)|^2 dr \quad (4)$$

Tissue losses is dominated by relaxation losses, which occurs at high frequency when the polarization of the dielectric material cannot follow up the change of applied electric field, the time lag in between results in energy dissipation(e.g. heat). Debye relaxation model and its variants are mainly used to describe the relaxation response of biological tissue[29].

The efficiency can be thus described as:

$$\eta = \frac{P_r}{P_{loss}} \quad (5)$$

The result from this study shows that, for most of the biological tissues, the optimal frequency occurs at GHz range. When the distance is at centimeter level and the frequency is at low GHz range, the field has both reactive and radiative modes. The configuration is in between the Near-field and Far-field. Because the wavelength is comparable to the distance, there's a possibility to apply constructive or destructive interference technique on the propagating EM waves to create a focused EM field.

The next step of the study was thus expanded from using a point source to finding a planar optimal source configuration. In both[30] and[31], the source was assumed to be a matrix of electric current density. Each current contribute to the final EM, field in the tissue. The EM field at receiver point is described by applying Green's function. Greens' function is the impulse response that correlates current density with EM field[32].

$$E_1(r) = i\omega\mu \int \bar{G}_E(r - r') J_1(r') dr' \quad (6)$$

$$H_1(r) = \int \bar{G}_H(r - r') J_1(r') dr' \quad (7)$$

$\bar{G}_E$  and  $\bar{G}_H$  are the Green's function for  $E$  field and  $H$  field respectively. The calculation process starts by converting the equation into the frequency domain by using Fourier transform. Thus the efficiency on the frequency domain become:

$$\gamma = \frac{\omega\mu_0^2 A_r^2 \left| \int \bar{\mathcal{G}}_H(z_f) \hat{n} \cdot \mathcal{J}_1 dk_s \right|^2}{4\pi^2 \int \mathcal{J}_1^* (\int Im \mathcal{E} \bar{\mathcal{G}}_E^*(z) \bar{\mathcal{G}}_E(z) dz) \mathcal{J}_1 dk_s} \quad (8)$$

Where the  $\mathcal{G}_H$  and the  $\mathcal{G}_E$  are the Green's function in frequency domain.  $\mathcal{J}$  is the current density in the frequency domain.

For this form of ratio, Cauchy-Schwarz inequality was used to calculate the  $J$  distribution that maximize the efficiency. In[30], the result shows that the magnitude of the optimal current density distribution decays rapidly as the dimension increases, suggesting that an optimal source can be closely represented within a finite dimension. In the main article, this process is done by assigning a 21-by-21 matrix of electric current density.

In summary, the theory of Mid-field wireless power transfer starts from removing the quasi-static approximation. The optimal operating frequency was recalculated so as to maximize the power transfer efficiency from a point source. Tissue losses were described by the Debye relaxation model. The optimal source was further represented by a matrix of current density distribution. The optimal magnitude and phase information of each current was calculated with the help of Green's function.

## APPENDIX B

### THE CODE OF OPTIMIZATION CALCULATION IN MATLAB

This appendix shows the main codes used in Matlab for optimal frequency and current density distribution calculation. The original code can be found in[15]. It provides three optimization methods based on the three constraints discussed in[28]. Here, only the total tissue losses constraint was taken into consideration and adjusted to fit the project in the main article.

The codes can be divided into four functional steps: Specification, Coupling factor calculation, Source calculation, and the Field solver.

#### A. Specification

This code is used to define all the parameters in the simulation environment: frequency, the tissue layer and tissue type, constraint for optimization, focal point, and the resolution. It can be seen as the foundation for other codes.

The tissue type is defined by assigning the dielectric constants. Parameters including relative permittivity and conductivity can be found from the study conducted by Gabriel in 1996 [17] and its online database in[33], an example of the dielectric parameters of the breast fat across a wide frequency range (10Hz-100GHz) is shown in Fig.20.

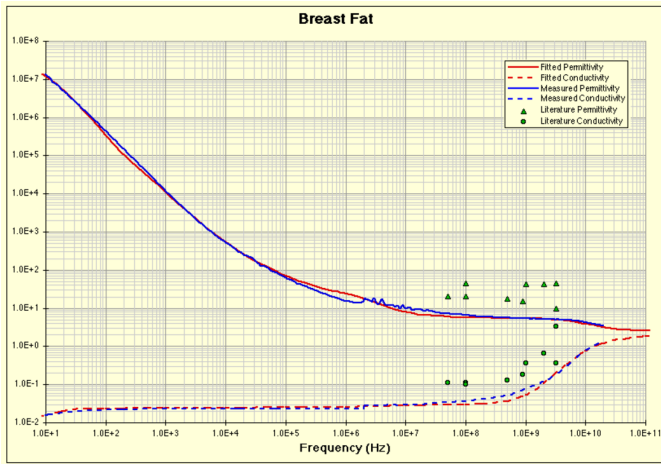


Fig. 20: The dielectric properties of the breast fat according to [17].

A table that lists the dielectric properties of different tissues were created and loaded into the code first. Next,

an array is created to store the tissue layer information by assigning their corresponding sequence number in the table as shown below:

```
1 ...
2 idxSkin = 33;
3 idxFat = 10;
4 idxGland = 30;
5 idxMuscle = 30;
6
7 %33 is the corresponding sequence ...
   number of 'skin' in the table,
8 %10 is the corresponding sequence ...
   number of 'breast fat' in the table,
9 %same principle apply to the gland ...
   tissue and muscle.
10 ...
```

Gland tissue was not included in the original codes, so the dielectric properties of the gland tissue were manually imported using the data extracted from[33], as shown below:

```
1 ...
2 switch(freq)
3     case(8e8)
4         epsR(4) = 5.99e+1;
5     case(1e9)
6         epsR(4)=5.95e+1;
7     case(1.2e9)
8         epsR(4)=5.91e+1;
9     case(1.4e9)
10        epsR(4)=5.88e+1;
11    case(1.6e9)
12        epsR(4)=5.84e+1;
13
14 %'freq' is the frequency of interests
15 %'epsR' is the relative permittivity of ...
   the gland tissue.
16 %The frequency points was set from ...
   800MHz to 4GHz.
17 ...
18
```

The resolution is also important for the calculation. In this code, the resolution is defined by specifying the interval for integration, the matrix size of the source, and the numbers of points in the frequency domain.

```
1 ...
2 numSrc = 21;
3 lenSrc = 0.061;
4 dSrc=lenSrc/(numSrc-1);
5 startSrc = -lenSrc/2+dSrc/2;
6 endSrc=lenSrc/2-dSrc/2;
7
8 %source parameters
```



```

9 %numSrc define that the total number of ...
  current elment in the matrix is ...
  numSrc^2
10 %lenSrc define the actual length of ...
  each grid
11 ...

```

```

1 ...
2 numxGridEVAL = ...
  floor(lenxGridEVAL/dxGridEVAL);
3 lenxGridEVAL = dxGridEVAL*numxGridEVAL;
4 startxGridEVAL = ...
  -lenxGridEVAL/2+dxGridEVAL/2;
5
6 numyGridEVAL = ...
  floor(lenyGridEVAL/dyGridEVAL);
7 lenyGridEVAL = dyGridEVAL*numyGridEVAL;
8 startyGridEVAL = ...
  -lenyGridEVAL/2+dyGridEVAL/2;
9
10 numzGridEVAL = ...
  floor(lenzGridEVAL/dzGridEVAL);
11 lenzGridEVAL = dzGridEVAL*numzGridEVAL;
12
13
14 % This section defines the numbers of ...
  points used to calculate the EM ...
  field in a 103*103*40 3D matrix, ...
  which represent the tissue volume.
15 %Same methods was applied to define the ...
  numbers of points used for integral ...
  operation, which are 201*201*400 ...
  points.
16 ...

```

## B. Coupling factor calculation

Once the parameters are defined, one can start the calculation of coupling factor. There are three main steps: First, define the Green's function for both electric field and magnetic field. Next, define the tissue losses and induced *emf* for each frequency point based on Equation(3) and Equation(4) described in Appendix A. Finally, integrate the results and calculate the corresponding coupling factor for each frequency point.

```

1 ...
2 genGreenMulti;
3 for zIdx = 1:numzGridDENSE
4   GeSquare(:, :, kxIdx, kyIdx, zIdx) = ...
5     (GeFull(:, :, kxIdx, kyIdx, ...
6       zIdx))' * GeFull(:, :, kxIdx, kyIdx, ...
7       zIdx);
8 end
9 imag(epsRMatrix).*reshape(GeSquare...
10 (:, :, kxIdx, kyIdx, :), 3, 3, numzGridDENSE);
11 F(:, :, kxIdx, kyIdx) = ...
  dzGridDENSE*sum(dF, 3);

```

```

10
11 %Define the Green's function for both E ...
  field and H field.
12 ...

```

```

1 ...
2 dPloss(kxIdx, kyIdx) = (Sopt(:, kxIdx, ...
3   kyIdx))' * F(:, :, kxIdx, kyIdx) * Sopt(:, ...
4   kxIdx, kyIdx);
5
6 dV12(kxIdx, kyIdx) = ...
  exp(1i*kx(kxIdx)*xFoc + ...
  1i*ky(kyIdx)*yFoc) * ...
  (h(:, kxIdx, kyIdx))' * ...
  Sopt(:, kxIdx, kyIdx);
7
8 %The tissue losses and induced emf ...
  calculation
9 ...

```

```

1 ...
2 Ploss = sum(sum(dPloss))*dkGrid^2;
3 V12 = sum(sum(dV12))*dkGrid^2;
4 emfSquare = (abs(V12))^2;
5 effcOpt = sum(sum(deff))*dkGrid^2
6
7 %The integration operation for both ...
  tissue losses and induced emf.
8 %effcOpt is the coupling efficiency ...
  calculation.
9 ...

```

The result of this part gives a relationship between the coupling factor and the frequency, which was then used to find the optimal frequency that gives the maximal coupling factor. An example of the result is shown in Fig.21, that the optimal frequency is at around 2.8GHz.

## C. Source calculation

This part is done after the optimal frequency has been determined. The calculation process shown below corresponds to one frequency. The current density at each point of the matrix was in the frequency domain, therefore the first step of this section is to apply an inverse Fourier transform on the result. Finally, the result was plotted using Quiver function in Matlab. The final output is shown in Fig.11 in the main article.

```

1 ...
2 FJxOpt(:, :) = Sopt(1, :, :);
3 FJyOpt(:, :) = Sopt(2, :, :);
4
5 for xIdx=1:length(srcx)
6   for yIdx=1:length(srcy)

```

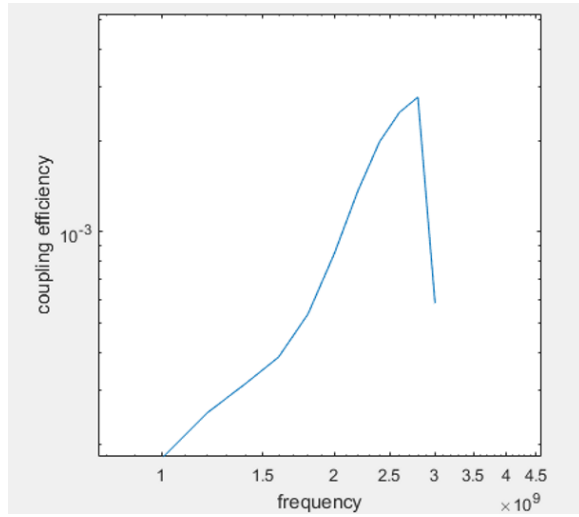


Fig. 21: The coupling factor versus frequency in a multilayered breast tissue model.

```

7  expTerm = ...
    1./4/pi^2*exp(1i*expkx.*srcx(xIdx) ...
8  +1i.*expky*srcy(yIdx))*dkGrid^2;
9  JxOpt(xIdx,yIdx) = sum(sum( ...
    FJxOpt.*expTerm ));
10 JyOpt(xIdx,yIdx) = sum(sum( ...
    FJyOpt.*expTerm ));
11
12 %The optimal current density that ...
    calculated in the previous section ...
    was in frequency domain,
13 %An inverse fourier transform is needed ...
    for a time-domain result
14 %The Jx and Jy in the 21-by-21 matrix ...
    is later visualized by using quiver ...
    function.
15 ...

```

#### D. Field solver

The field solver is based on the Equation(6) and Equation(7) described in the Appendix A. By integrating the product of Green's function and current density at each point, the magnetic field and electric field can be obtained. As previously described in the section of resolution, the Z axis was divided into 400 points, each point represent a layer of the tissue volume with 201x201 points. During the calculation, the EM field at each layer was calculated in sequence.

```

1  ...
2  for zIdx = 1:length(z)
3  zFoc = z(zIdx);

```

```

4  genGreen;
5  for kxIdx=1:length(kx)
6  for kyIdx=1:length(ky)
7  FE(:,zIdx,kxIdx,kyIdx)=Ge(:, :, kxIdx, ...
8  kyIdx)*SUT(:, kxIdx, kyIdx);
9  FH(:,zIdx,kxIdx,kyIdx)=Gh(:, :, kxIdx, ...
10 kyIdx)*SUT(:, kxIdx, kyIdx);
11 end
12 end
13 end
14
15
16 %A loop to calculate the EM field at ...
    each layer in the spatial frequency ...
    domain.
17 ...

```

```

1  ...
2  for zIdx=1:length(z)
3  for xIdx=1:length(x)
4  for yIdx=1:length(y)
5  expTerm = ...
        1./4/pi^2*exp(1i*expkx.*x(xIdx)+...
6  1i.*expky*y(yIdx))*dkGrid^2;
7  FTemp(:, :) = FE(1,zIdx, :, :);
8  Ex(xIdx,yIdx,zIdx) = sum(sum( ...
        FTemp.*expTerm ));
9  FTemp(:, :) = FE(2,zIdx, :, :);
10 Ey(xIdx,yIdx,zIdx) = sum(sum( ...
        FTemp.*expTerm ));
11 FTemp(:, :) = FE(3,zIdx, :, :);
12 Ez(xIdx,yIdx,zIdx) = sum(sum( ...
        FTemp.*expTerm ));
13 FTemp(:, :) = FH(1,zIdx, :, :);
14 Hx(xIdx,yIdx,zIdx) = sum(sum( ...
        FTemp.*expTerm ));
15 FTemp(:, :) = FH(2,zIdx, :, :);
16 Hy(xIdx,yIdx,zIdx) = sum(sum( ...
        FTemp.*expTerm ));
17 FTemp(:, :) = FH(3,zIdx, :, :);
18 Hz(xIdx,yIdx,zIdx) = sum(sum( ...
        FTemp.*expTerm ));
19 end
20 end
21 end
22
23 %The result of the frequency-domain EM ...
    field is converted into time domain ...
    for each axis.
24 ...

```

The calculated EM field in the form of matrix is shown below. In the main article, the result of EM field at the first layer was extracted and translated into the EM simulation software FEKO to represent the equivalent source. The conversion is done by adjusting the data for both E and H fields into \*.efe and \*.hfe files, the detailed requirement of these two files can be found in the user manual of FEKO at Section 3-21[34].

```

1  ...
2  save(fieldsFile, 'Ex', 'Ey', 'Ez', ...
   'Hx', 'Hy', 'Hz');
3  Ex1=Ex(:, :, 1);
4  Ey1=Ey(:, :, 1);
5  Ez1=Ez(:, :, 1);
6  Hx1=Hx(:, :, 1);
7  Hy1=Hy(:, :, 1);
8  Hz1=Hz(:, :, 1);
9
10
11 %The result is stored in the matrix.
12 ...

```

form as the \*.efe and \*.hfe files ...  
that can be recognized by FEKO. ...  
Same method can be applied to ...  
translate the data into another EM ...  
simulation software CST.

```

1  clear all;
2  load field_data.mat; % the calculated ...
   EM field is loaded.
3
4  Efile=zeros(103*103,9);
5  Hfile=zeros(103*103,9);
6
7  Exfile=zeros(103*103,5);
8  Eyfile=zeros(103*103,5);
9  Hxfile=zeros(103*103,5);
10 Hyfile=zeros(103*103,5);
11 Ezfile=zeros(103*103,5);
12 Hzfile=zeros(103*103,5);
13
14 zidx=1;
15
16 % only the first layer of the result ...
   was taken to represent the source
17
18 for xidx=1:1:103
19   for yidx=1:1:103
20
21     xx=(-0.0305)+((xidx-1)*(5.98039e-4));
22     yy=(-0.0305)+((yidx-1)*(5.98039e-4));
23
24 %scale the coordinates into a actual ...
   length. The side length of the ...
   source is 3.05cm*2=6.12cm, the ...
   spacing is around 6mm.
25
26 Efile((xidx-1)*103+yidx,:)= [xx,yy,zidx...
27 -1,real(Ex(xidx,yidx,zidx)),imag(Ex(...
28 xidx,yidx,zidx)),real(Ey(xidx,yidx,zidx...
29 )),imag(Ey(xidx,yidx,zidx)),real(Ez(xidx...
30 ,yidx,zidx)),imag(Ez(xidx,yidx,zidx))];
31
32 Hfile((xidx-1)*103+yidx,:)= [xx,yy,zidx...
33 -1,real(Hx(xidx,yidx,zidx)),imag(Hx(...
34 xidx,yidx,zidx)),real(Hy(xidx,yidx,zidx...
35 )),imag(Hy(xidx,yidx,zidx)),real(Hz(xidx...
36 ,yidx,zidx)),imag(Hz(xidx,yidx,zidx))];
37
38   end
39 end
40
41
42 %the data is adjusted into the ACSII ...

```

## APPENDIX C

### SIMULATION OF CURRENT DENSITY DISTRIBUTION IN FEKO

In this appendix, three different ways to simulate the current density distribution in Fig.11 were tested. The goal was to assign the magnitude and phases at each point. However, they are all not able to represent the source.

Three types of sources that were used to represent the matrix of current density distribution were:

- Electric dipoles matrix
- Multiple dipole arrays
- Impressed current paths

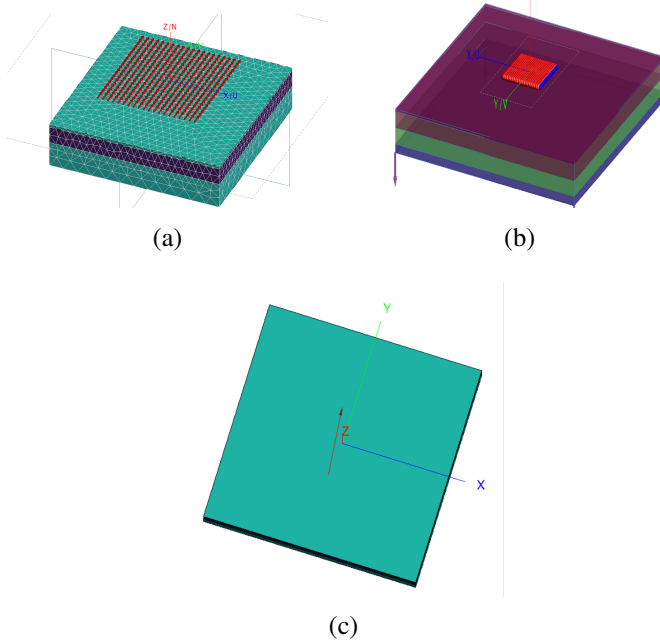


Fig. 22: Three attempts of representing the current density distribution. (a) Electrical Dipoles; (b) Multiple dipole arrays; (c) Impressed currents.

The dipoles in the first method, as shown in Fig.22a is for ideal dipoles, where the dimension is infinitely small. This agrees with the definition of a current density which is the electric current per unit area of a cross section. Each dipole was assigned with the individual magnitude and phase information successfully. However, FEKO was not able to distinguish between some dipoles even when they were all at different positions, the error occurred at 104 points out of 441 (21x21) points. The cause was

estimated to be the overlaying computational space of each dipole which is related to the magnitude inputs.

The second method, as shown in Fig.22b is realized by applying twelve parallel antenna arrays. In each array, there are twelve dipoles. The dipoles used in this method are not ideal as the first method, which means that a specified length needs to be assigned for each dipole. The length of the dipole and the spacing between the different arrays were set to be 2.8mm, so that the total dimension of the source was controlled at 6cm by 6cm. The first problem of this method is that it requires a huge amount of computation. Secondly, there is a significant coupling effect between each dipole that the antenna array will not produce the same EM field.

The third method, as shown in Fig.22c, is done by using impressed current. Impressed current models a segment of the current path. One can assign the magnitude and phase on both the starting point and ending point of a current path. The length and diameter of the current path can also be changed like the second method. However, according to the user manual of FEKO[34], FEKO is not able to accurately calculate the radiated power if multiple current paths are used.

In summary, three different ways of simulating current density distribution were tested, and they were not able to provide an accurate result. In the main article, the equivalent EM field was used to represent the source instead.

## APPENDIX D

### RESONANT FREQUENCY OF RECEIVER WITH TWO DIFFERENT COIL CONFIGURATIONS

The goal of this appendix is to conduct another test to show that the changes in resonant frequency depends on the coil configuration. In the main article, the result was that by winding the coil around the PCB, the resonant frequency of the receiver will decrease compared to that of a PCB with a separated coil. In order to remove the possible influences from the components, a naked PCB was used.

During the experiment, a conductive material was firstly wound around two naked PCBs with the same dimension (3mmx1mmx18mm). Next, an insulated plastic was wound around the conductive material to prevent electrical contact with the coil. Finally, a 5-turn coil was soldered onto the conductive material in two configuration as shown in Fig.23a and Fig.23b, where the first coil was wound around PCB, the second coil was separated from the PCB.

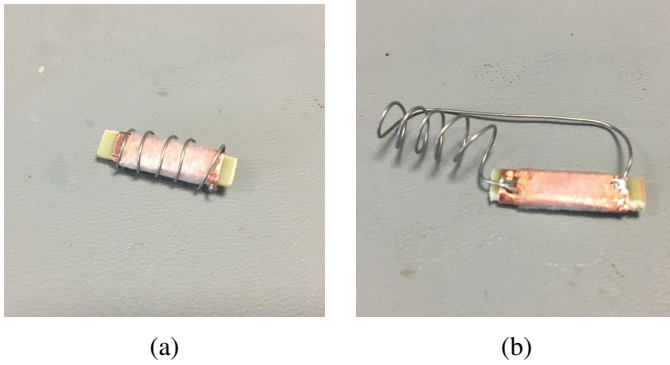


Fig. 23: Two receivers with two different coil configuration. (a) The coil was wound around the PCB; (b) The PCB was separated from the PCB

The resonant frequency of each receiver was tested by putting the receiver closely to a small loop antenna while its S11 parameter was measured by a network analyzer. The change in the S11 parameter reveals an energy coupling, and the corresponding frequency was taken to be the resonant frequency of the receiver.

The result is consistent with the main article that the PCB wound with coil has a lower resonant frequency (1.41GHz) than that of a PCB with a separated coil (2.10GHz).

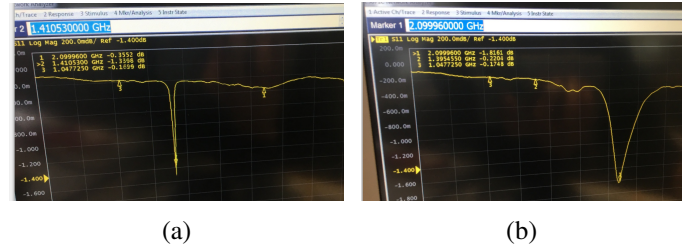


Fig. 24: The result of resonant frequency of two receivers. (a) The frequency was at around 1.41GHz when the coil is wound around the PCB; (b)The frequency was at around 2.10GHz when the coil is separated with the PCB.

## APPENDIX E

### THE DESIGN PROCESS OF THE RECEIVER

This appendix shows the complete process of the receiver circuit design and realization. As mentioned in the main article, the circuit should be able to provide sufficient voltage to the LED.

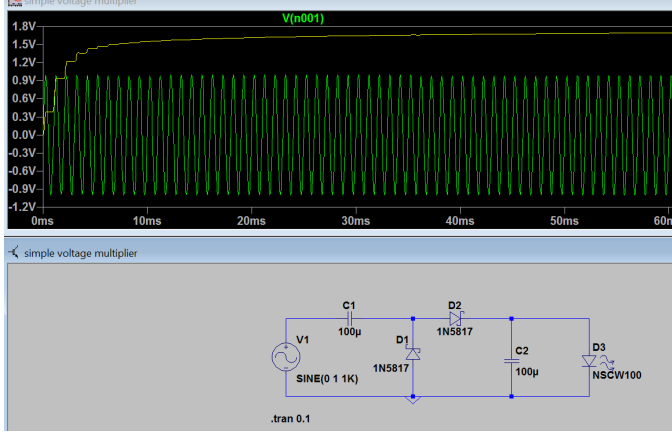


Fig. 25: The simulation result of a simple voltage multiplier. The AC input was 1V (1KHz), the rectified output was increased to 1.7V.

It first started by understanding the functionality of voltage multiplier. A simple model as shown in Fig.25 was simulated. The voltage source was operating at 1KHz. After a two-stage voltage multiplier, it can be seen that the output voltage increases from 1V to nearly 1.7V. It was recognized that there exists an internal resistance for each diode, so the more diodes in the circuit, the more power will be wasted before reaching the LED(load). If the input voltage is too small, the output voltage may not be increased due to the resistances in the diodes. In most cases, the input voltage harvested inside an implant is very weak. Hence it is important to decide upon the number of diodes used in the design of the multiplication circuit, which requires an estimated value of input voltage.

The input voltage estimation is done using both FEKO and Matlab. In FEKO, once the antenna, tissue model, and the input power are set, one can obtain both the Electric field and Magnetic field within a defined volume. It was assumed that a 5-turn coil with 2 mm diameter would be placed inside the tissue to couple the magnetic energy. According to Faraday's law, the voltage generated by the coil in a time-varying magnetic field can be described as:

$$V = -N \frac{\Delta(B \cdot A)}{\Delta t} = -N \Delta(B \cdot A) \cdot f \quad (9)$$

where the  $N$  is the turn number,  $B$  is the magnetic field,  $A$  is the area, and  $t$  is the time interval.

The induced voltage is proportional to the numbers of turn, the rate of change in the imposed magnetic field, and diameter of the coil. The volume was hence defined as a cylinder divided into 5 areas as shown in Fig.26 (in the red frame) to mimic a 5-turn coil. Each area has 945(21x45) measured points that records magnetic field along the X axis, Y axis, and Z axis. FEKO allows user to export the data of the magnetic field result for a further process, the form is as shown in Fig.27.

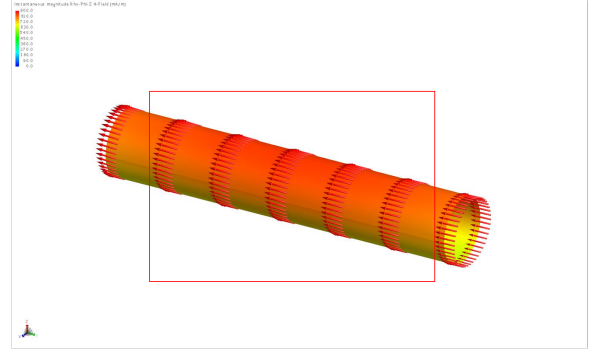


Fig. 26: In FEKO, the cylinder was divided into 5 areas (in the red frame) to record the magnetic field. The result mimics the magnetic flux passing through a 5-turn coil. The red arrows in the figure shows the direction of the magnetic field.

X	Y	Z	Re[Hz]	Im[Hz]	Re[Hz]	Im[Hz]	Re[Hz]	Im[Hz]
0.00000000E+00	0.00000000E+00	0.00000000E+00	4.49916865E-11	6.35693153E-12	-2.64327484E-03	-6.87638378E-02	-6.31253981E-01	7.14553933E-01
6.25000000E-05	0.00000000E+00	0.00000000E+00	-6.64233111E-05	4.43867767E-06	-2.64350267E-03	-6.87639951E-02	-6.31248708E-01	7.14552134E-01
1.25000000E-04	0.00000000E+00	0.00000000E+00	-1.32814588E-04	8.68377672E-06	-2.64416047E-03	-6.87611437E-02	-6.31232246E-01	7.14548221E-01
1.87500000E-04	0.00000000E+00	0.00000000E+00	-1.99117217E-04	1.32630125E-05	-2.64510932E-03	-6.87584878E-02	-6.31202095E-01	7.14544883E-01
2.50000000E-04	0.00000000E+00	0.00000000E+00	-2.65332225E-04	1.79298112E-05	-2.64660425E-03	-6.87546894E-02	-6.31161132E-01	7.14540321E-01
3.12500000E-04	0.00000000E+00	0.00000000E+00	-3.31541395E-04	2.26456484E-05	-2.64870638E-03	-6.87501179E-02	-6.31107629E-01	7.14534267E-01
3.75000000E-04	0.00000000E+00	0.00000000E+00	-3.97841059E-04	2.71724863E-05	-2.65146207E-03	-6.87443716E-02	-6.31041879E-01	7.14527079E-01
4.37500000E-04	0.00000000E+00	0.00000000E+00	-4.64204452E-04	3.14237033E-05	-2.65467770E-03	-6.87379168E-02	-6.30963345E-01	7.14519985E-01
5.00000000E-04	0.00000000E+00	0.00000000E+00	-5.30533897E-04	3.58954316E-05	-2.65833124E-03	-6.87301950E-02	-6.30873940E-01	7.14510425E-01
5.62500000E-04	0.00000000E+00	0.00000000E+00	-5.96839152E-04	4.01282886E-05	-2.66240966E-03	-6.87210084E-02	-6.30773822E-01	7.14497558E-01
6.25000000E-04	0.00000000E+00	0.00000000E+00	-6.63060422E-04	4.46129720E-05	-2.66684820E-03	-6.87106962E-02	-6.30662259E-01	7.14482918E-01
6.87500000E-04	0.00000000E+00	0.00000000E+00	-7.29180577E-04	4.92403470E-05	-2.67146465E-03	-6.86996069E-02	-6.30537614E-01	7.14468885E-01

Fig. 27: The exported data describing the magnetic field information at each point. The data includes the coordinates, the real and imaginary part of the magnetic field along different axis

This data can then be easily translated into Matlab and is used for voltage calculation. The coil only harvests energy along one direction. In this study, the direction is along Y axis. Hence, during the voltage calculation,



only the magnetic flux along the Y axis on each area was used, which are the sixth and seventh column of data in Fig.27.

The total voltage generated in the coil is approximately the sum of the five induced voltages. The input voltage was found to be at a level of few hundred millivolts.

This result was later applied in the circuit design. In LTSPICE, a 500 mV AC voltage was assumed to be the input of the circuit. The configuration of four diodes and four capacitors as the voltage multiplier was found to be optimal for a sufficient output voltage. In order to remove the rippling voltage on the LED, another capacitor is added in parallel to the LED.

The circuit was tested first on a single layer PCB, the layout is shown in Fig.28. Three pairs of soldering pads were placed on the PCB for a higher robustness so that one can solder and de-solder the coil several times for different tests.

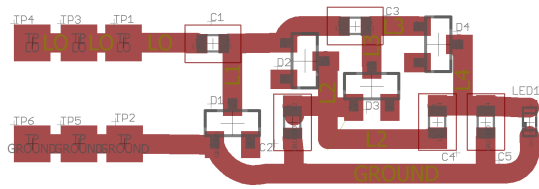


Fig. 28: The circuit layout of the LED marker on the single layer PCB.

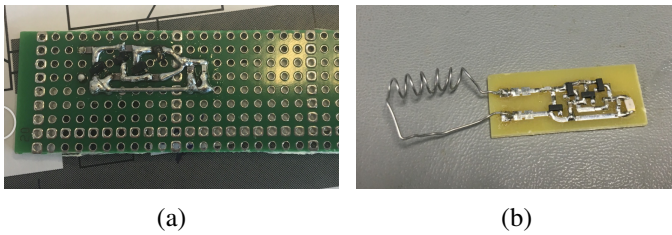


Fig. 29: The implementation of the circuit designed on the single layer PCB. (a) The components were soldered on a perfboard first; (b) The components were soldered on the customized PCB.

The circuit was first implemented on a perfboard as shown in Fig.29a, and then onto a customized PCB as in Fig.29b.

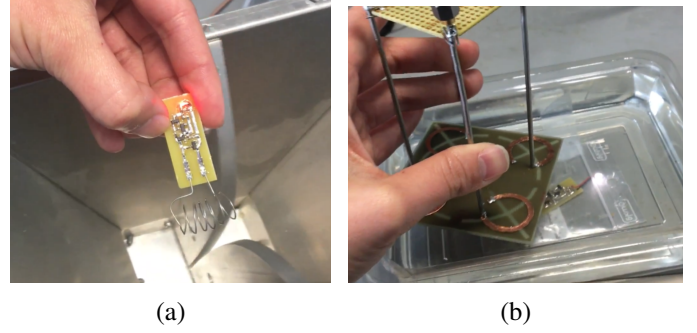


Fig. 30: The experimental results of the LED marker on the single layer PCB. (a) The LED marker is powered up by coupling energy from the horizontal magnetic field produced by a broad-band EM antenna; (b) The LED maker is powered up under the tissue simulating liquid by the 4-port antenna.

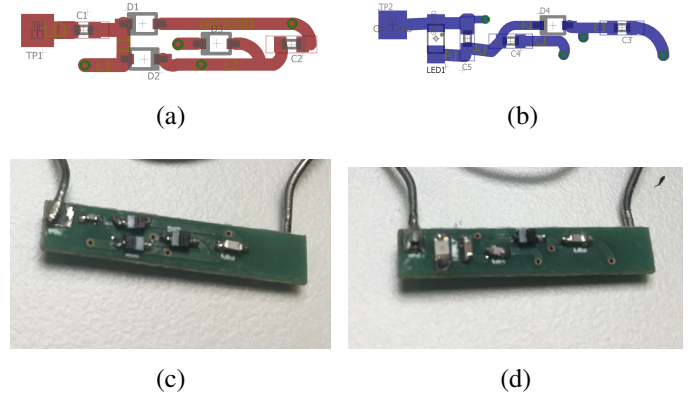


Fig. 31: The circuit layout and the realization of the double-layer PCB. (a) The top view of the circuit layout; (b) The bottom view of the circuit layout; (c) The top view of the implemented PCB; (d) The bottom view of the implemented PCB.

The purpose of using the single layer PCB was to verify the function of the designed circuit. Hence, the size of the PCB is still at centimeter level. In Fig.30a, the LED marker was placed above a broadband EM antenna and the coil was harvesting the magnetic energy in the horizontal direction. Later, it was placed under the tissue simulating liquid and powered up as shown in Fig.30b. In the second test, the LED was replaced by a white LED which has a higher light intensity.

These results verified that the circuit was able to

TABLE I: The list of all the components

Components	D1-D4	C1,C5	C2-C4	LED
Series number	BAT 15-03W E6327	MCHH15N101J500CT	CBR04C470J5GAC	KPT-1608SECK-J3
Value	N/A	100 <i>pf</i>	47 <i>pf</i>	N/A
Company	INFINEON	MULTICOMP	KEMET	KINGBRIGHT
Package	SOD323	0402	0402	0603

convert the magnetic energy into sufficient electrical energy to power up the LED. Therefore, the next step was to minimize the size of the PCB by applying double layer PCB design. The top view and bottom view of the double layer PCB design are shown in Fig.31. Most of the components were chosen to be as small as possible. The packages of the components were either 0603 or 0402, as shown in TABLE.I. The final dimension of the entire PCB was decreased to 1mmx3mmx20mm.

Soldering pads in the double-layer PCB were put at both ends on both sides so that it would be possible to have the coil wound around the PCB. This PCB was used in the final experiment as described in the main article. The size of the PCB can be further minimized by using application-specific integrated circuit design, which could be costlier and was not considered in this study.

In summary, the design process of the LED marker starts by estimating the input voltage of the circuit, then to decide the numbers of voltage multipliers, and finally the implementation with both single-layer PCB design and double-layer PCB design.

## APPENDIX F

### A PROPOSAL OF QUANTIFYING THE REQUIRED INPUT POWER FOR AN IMPLANTED LED TO BE DETECTABLE.

Quantifying the level of required power is important in wireless power transfer design. Because different tissue has different optical properties, the same amount of input power may end up with very different visibility from the skin level. In the main article, this is shown by comparing the light intensity of the inserted LED in the slab of butter and in the swan lung tissue. The light is seen to be much more visible when it's in the butter, whereas it is only visible in a dark environment for the case of Swan lung tissue. Hence, it's important to evaluate the required input power of the LED for a sufficient visibility.

This appendix propose a quantification method that measures the level of visibility of a LED under a certain thickness of tissue, and at the same time correlate the visibility with the LED input power.

The experimental components required are: a wire-powered LED, a power source, the tissue to be investigated, and a photometer, as shown in Fig.32.

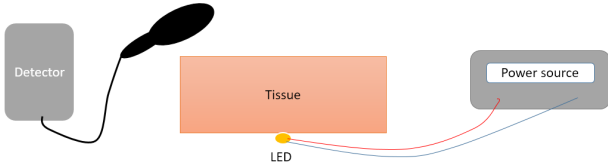


Fig. 32: The set-up for power measurement and light intensity measurement

The LED is powered by connecting it to the power source. The power source displays the voltage and current supplied to the LED. Based on this information, one can directly calculate the input power of the LED by multiplying the voltage and current.

The light intensity is measured by placing the photometer above the tissue. A Photometer is an instrument that measures light intensity or the optical properties of solutions or surfaces[35].

The first step is to define a value of light intensity that can be classified as 'visible'. Here, this value is called 'visible threshold'. It guarantees that regardless of the variants of tissue types, once the light emitted from the LED placed inside the tissue is higher than the visible threshold, it should be detected by the naked eye.

Another important parameter to be taken into consideration is the depth of implantation. Different depths of the targeted lesion in different tissues require different input power to reach the same visible threshold. A table that can be used to record the required input power is shown in Fig.33.

Depth (cm)	Fat	Liver	Lung
2	e.g. 500uW		
3			
4			
5			

Fig. 33: An example of table that can be used to record the power requirement of the LED to be visible in different tissue type with different depths

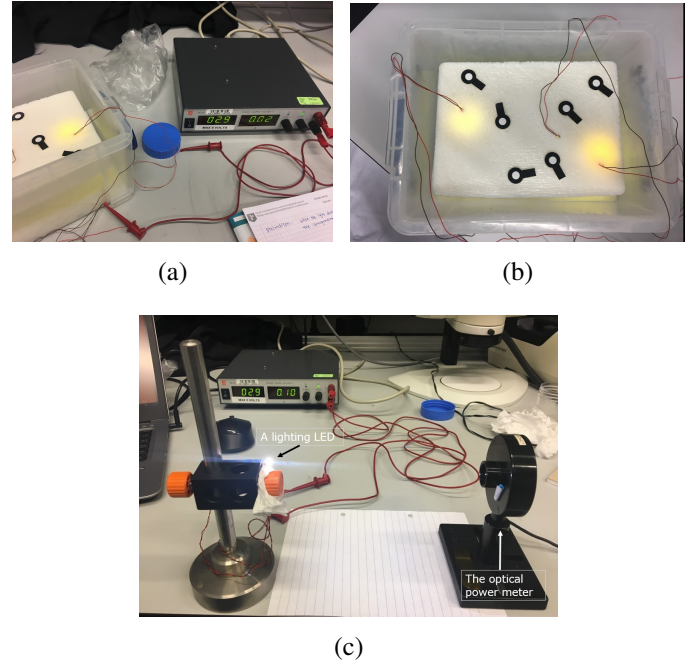


Fig. 34: The experimental set-up to quantify the relation between light intensity and input power. (a) The power source and the LED inserted in a phantom model; (b) The light spots seen on the top of the phantom; (c) The optical power meter is measuring the light power of a LED.

By using the data from the table, it become intuitive to decide the input power level and the number of LEDs required for a certain application. In fact, this should be the first step of designing a wireless powered LED

marker for intraoperative localization, so that during the circuit design phase, the input power of the transmitter and the number of stages for voltage multipliers can be determined based on the power requirement.

During the experimental set-up, it was tried to carry out a same experiment. The LEDs were inserted into a phantom model and connected with a power source as shown in Fig.34a. When the LEDs light up with a total input power of 0.058W, the light spots seen on the top were very clear as shown in Fig.34b. This light intensity can be considered as sufficiently visible used as a localization guidance. An optical power meter was placed on the table aiming at a lighting LED to quantify its light intensity as shown in Fig.34c. Unfortunately, the optical power meter we had is very sensitive to temperature, so it was difficult to obtain an accurate result by holding the optical power meter above the surface of the phantom model. One potential solution would be to replace the optical power meter by a handheld photometer.